Effects of Microstructural Changes on Mechanical Properties in Ferritic-Martensitic Alloys

A Thesis

Presented in Partial Fulfillment of the Requirements for the

Degree of Master of Science

with a

Major in Mechanical Engineering

in the

College of Graduate Studies

University of Idaho

by

Matthew D. Harned

Major Professor: Matthew Swenson, Ph.D., PE

Committee Members: Michael Maughan, Ph.D., PE; Gabriel Potirniche, Ph.D., PE

Department Administrator: Steven Beyerlein, Ph.D.

August 2019

Authorization to Submit Thesis

This thesis of Matthew D. Harned, submitted for the degree of Master of Science with a Major in Mechanical Engineering and titled "Effects of Microstructural Changes on Mechanical Properties in Ferritic-Martensitic Alloys," has been reviewed in final form. Permission, as indicated by the signatures and dates below, is now granted to submit final copies to the College of Graduate Studies for approval.

Major Professor: _____   Date: _____

         Matthew Swenson, Ph.D., PE

Committee Members: _____   Date: _____

         Michael Maughan, Ph.D., PE

                          _____   Date: _____

         Gabriel Potirniche, Ph.D., PE

Department

Administrator: _____   Date: _____

         Steven Beyerlein, Ph.D.

Abstract

As an important part of the design and development of advanced nuclear fission and fusion reactors, nuclear materials research is focused on finding materials that will perform under the high temperatures, high radiation doses, and corrosive environments predicted for these reactors. Highly alloyed ferritic-martensitic steel alloys show promise as fuel cladding and reactor core structural materials for their high-temperature performance, resistance to swelling, embrittlement, and oxidation, and relatively low nuclear radioactivation.

Microstructural damage due to irradiation, including dislocation loop and cluster formation, can affect the mechanical properties. The objective of this study is to correlate irradiation-induced damage in the microstructure of two ferritic-martensitic steel alloys to a change in yield strength. Two candidate materials for use in advanced Gen IV reactors, HCM12A and HT-9, were previously irradiated with Fe^{2+} ions to 3 displacements per atom (dpa) at 500°C, and a sample of the HCM12A was also irradiated with to 2.4 dpa with protons. Prior published microstructural data from a transmission electron microscopy (TEM) study of the samples was used, including changes in the number density and diameter of dislocation loops and nanoclusters, and changes in the atomic concentration of various solutes in the matrix. Nanoindentation was performed on all samples to determine the change in hardness as a result of the irradiation. A quasi-static indentation technique with a Berkovich indenter tip was used, and the hardness was measured to a depth of 600 nm in each sample. A two-feature dispersed barrier hardening (DBH) model was implemented in conjunction with solid solution hardening to mathematically correlate the changes in microstructure to the changes in hardness and yield strength by solving for the strengthening coefficients of the DBH model.

In the Fe^{2+}-irradiated HT-9, no nanoclusters were observed and thus no change in solid solution composition took place; only loops were detected, which caused an increase in yield strength of 9.3%. Loops and nanoclusters were observed in both the Fe^{2+}- and proton-irradiated HCM12A; both linear and RSS superposition methods were used to combine the effects of loops and nanoclusters. The Fe^{2+}-irradiated HCM12A sample experienced an increase in yield strength of 23%, and the proton-irradiated sample strength increased by 11%.

Acknowledgements

I would like to express my thanks to Dr. Matthew Swenson, my major professor, for his support, investment, instruction, and patience on this project. Thanks also to KLA-Tencor and Marzyeh Moradi for their collaboration in this research and expertise in nanoindentation.

Thanks to Dr. Mike Maughan for his help with some of the concepts discussed in this thesis, and to both he and Dr. Gabriel Potirniche for their input and comments as members of my review committee.

Thanks to the professors, staff, fellow graduate students, and undergrads I've been privileged to work with in the Mechanical Engineering department during my studies here.

Finally, thanks to my parents, my parents-in-law, and my wife for their ongoing support and encouragement along the way.

Table of Contents

List of Tables

List of Figures

Chapter 1: Introduction

With rising global demand for low-cost clean energy, nuclear fission and fusion systems will become increasingly important energy sources for both economic and environmental reasons. Advanced systems will operate at higher efficiency, requiring materials to be long-lasting and durable, and have excellent high-temperature performance under adverse conditions. Qualities such as resistance to oxidation, resistance to swelling, and low levels of radioactivation will be critical for any material used in nuclear reactor components, specifically fuel cladding or structural elements surrounding the reactor core. Materials research has historically focused on austenitic stainless steels, superalloys, or ferritic-martensitic (F-M) steels. Two alloys of the latter category, HCM12A and HT-9, are the subjects of this study.

In theory, the neutron flux emanating from the reaction in the core of a power plant can be estimated; that is, the exposure to radiation experienced by a component over time can be estimated with some degree of confidence. Furthermore, there are methods to estimate the microstructural damage incurred by a material as a function of exposure to radioactivity, so reasonable predictions can be made as to the level of microstructural damage accrued over time in a component in a nuclear facility. What is less understood, however, is how the nano- or micro-level changes effect the bulk properties of the material or harm its performance. This study seeks to quantify microstructural damage resulting from exposure to radiation, and correlate this damage to changes in the yield strength.

High-temperature and high-dose radiation conditions exist in nuclear power systems, and this environment can adversely affect material properties and performance. High-energy particles bombard the atoms in the steel matrix, causing damage at the atomic and intermediate scale. Dislocation lines can intersect and wrap around an obstacle, forming dislocation loops. Alloying elements can cluster together and form nanoparticles distinct from the bulk solution. Vacancies can form and coalesce, becoming voids within the metal; these bubbles or pockets can cause the metal to swell and distort, compromising dimensional stability. All these microstructural damages add up, causing changes to the bulk material properties.

F-M steels display excellent high-temperature strength and resistance to radiation-induced swelling [1]. The aim of this study is to develop a correlation between changes in the microstructure and changes in the yield strength of two ferritic-martensitic (F-M) alloys. Typically, radiation

damage will cause alloys to become harder, stronger, and more brittle. Mathematical models have been developed to predict hardening/strengthening as a function of the damage features' diameter and volumetric density, notably the dispersed barrier hardening model. This study follows these experimental and analytical steps:

- High-temperature irradiation of material samples to a known damage level
- Microstructural characterization of the materials, in both the as-received and irradiated conditions
- Nanohardness testing of the surface layer in both the as-received and radiation-damaged samples
- Mathematical analysis correlating changes in microstructure to changes in hardness/strength

 A model is suggested that accounts for loops, nanoclusters, and solid solution hardening, and the constants in the dispersed barrier hardening model are solved for.

Chapter 2: Background

Nuclear Applications

As the global demand for abundant, affordable, and clean energy grows, nuclear fission and fusion will become more widespread and more important in the industrialized world. In fission reactors, the nuclei of a refined actinide isotope (typically uranium or plutonium) is impacted by a neutron, splitting the atom into daughter nuclei and releasing both energy and several more neutrons capable of splitting other fuel atoms in an ongoing, controlled chain reaction. The neutron radiation produced by this process, and the high temperatures associated with the reaction, also affect the structural elements and fuel containment cladding of the reactor. Therefore the materials used to build the reactor must perform well at these temperatures and be resistant to adverse effects from neutron radiation. Advanced reactors are expected to operate at temperatures up to 700°C and produce neutron radiation doses up to several hundred displacements per atom (dpa) [2]. Historically, austenitic stainless steels were the material in focus, but are considered to be ineffective due to a tendency to swell under neutron flux, and because their low thermal conductivity and high thermal expansion coefficient can too easily cause stresses or distortion at higher temperatures [3]. Various refractory metals or superalloys have also been considered, but these are generally too easily activated in the presence of radioactivity, which can render disposal difficult and expensive. The F-M alloys discussed in this study are examples of "reduced-activation" materials, meaning that they are activated (become radioactive) only to a degree such that they can be disposed of by shallow land burial [3].

High-chromium (9-12%) ferritic alloys have been manufactured and studied for over a century, and have been in use in energy production, chemical plants, and other high-temperature applications; they have been incorporated into boilers and turbines, and are presently in use in fission reactors [3]. These materials are low-carbon body-centered cubic (bcc) steels that have been highly alloyed for optimum performance in these harsh conditions. Furthermore, these alloys are designed for decreased residual radioactivity by the avoidance or minimization of certain elements that have longer decay or "cool-down" periods; these alloys are called "reduced activation" and they are safer for personnel to work with, and easier and cheaper to dispose of.

The high-chromium ferritic or F-M steels have much lower rates of swelling under neutron radiation than austenitic stainless, and unlike the vanadium alloys or silicon carbide/SiC composites, can be readily cast, forged, and welded [3]. These properties make it an ideal material for use in

future fusion reactor designs, where the two primary issues to be solved involve the presence of ferromagnetic materials interfering with the magnetic containment of the plasma, and the effect of neutron irradiation on the mechanical properties.

F-M Steels HCM12A and HT-9

The important and useful properties that high-chromium steels possess, namely corrosion resistance, strength, ductility, toughness, and resistance to activation, swelling, or embrittlement under radiation, are due to both a) the elemental composition and concentration of solutes and b) the grain structures/phases present. The phase is affected by both the composition and the cooling rates and heat treatments.

Alloys below about 12 wt% Cr become completely austenitized when heated to the austenitization temperature range of 850 to 1250°C [3]. Austenite is a face-centered cubic (FCC) structure which is transformed to martensite, a body-centered cubic (bcc) structure when quickly cooled to room temperature. At concentrations of chromium above 12%, some or all of the alloy can remain in the ferrite phase, leaving the cooled alloy with some δ-ferrite present. The martensite phase is generally stronger and tougher than the δ-ferrite phase [3]; thus, it becomes a balancing act to include sufficient concentration of chromium to achieve the strength and high-temperature performance necessary without including too much and leaving the alloy with a too-significant fraction of δ-ferrite. The Fe-Cr phase diagram for a 0.1% C alloy is shown in the figure below [3].
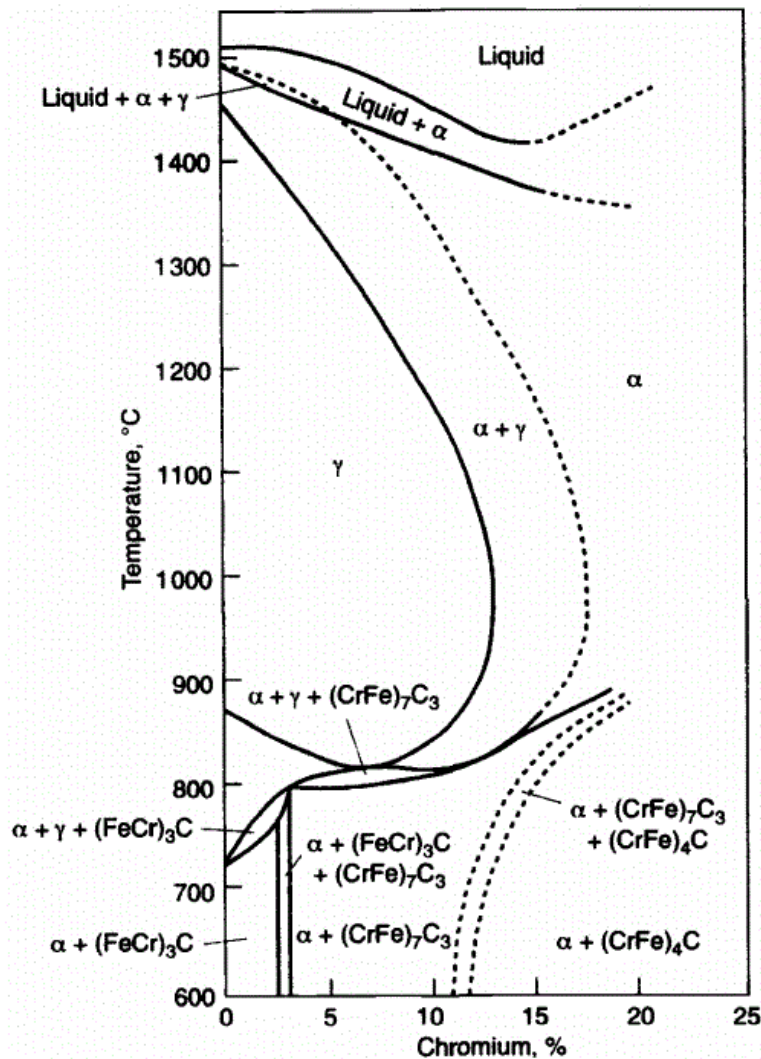
Figure 2.1. Chromium phase diagram for low-carbon (0.1% C) Fe-Cr-C alloys, from [3].

The γ (austenite) loop can be shifted to the right by adding or increasing the concentration of the austenite-forming elements, including C, N, Ni, Mn, Cu, and Co. These are known as nickel-equivalent alloying components, and can facilitate the formation of austenite phase at higher concentrations of chromium. The disadvantage, however, is that some of these elements, notably Ni, are less desirable because they tend to retain harmful levels of radioactivity for a longer time [3]. The formation of austenite is inhibited by the addition of the ferrite-forming elements V, Nb, Ta, Ti, and Al, which shifts the γ-loop to the left. These elements are called chromium-equivalent components, and tend to increase the amount of δ-ferrite that remains in the alloy. Alloys such as HCM12A that contain both martensite and ferrite structures at room temperature are known as 'duplex' alloys.

Furthermore, in the case of HT-9, there are three different structures present; δ-ferrite, martensite laths, and some "islands" of remaining austenite incompletely transformed to martensite [3]. These phases are organized and compared in the Schaeffler-Schneider diagram below, from [4].
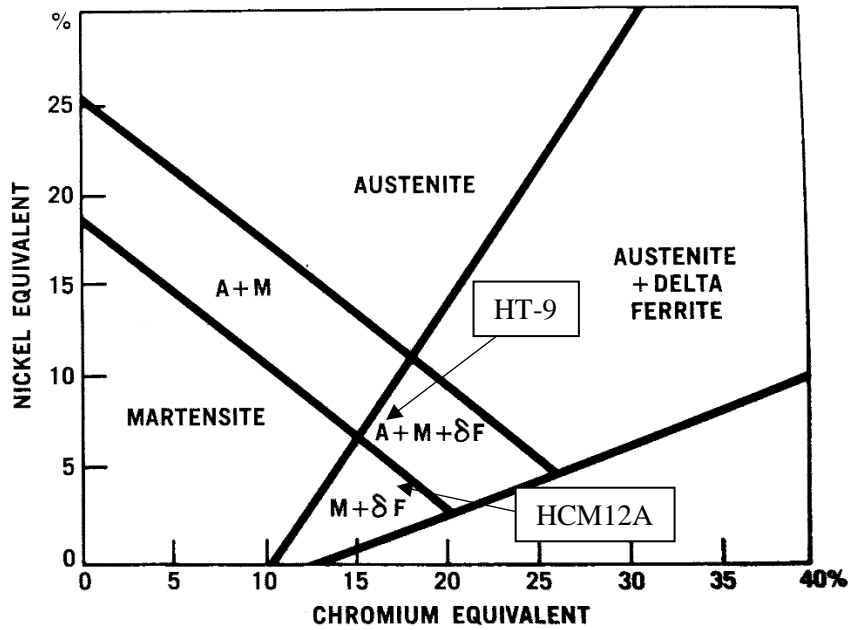
Figure 2.2. Schaeffler-Schneider diagram showing phase transformation as a function of alloying elements [4].

HCM12A is a duplex alloy, located at about 15% Cr equivalent and 6% Ni equivalent on the above diagram, while HT-9 is a three-phase alloy, retaining some austenite at about 15% Cr equivalent and 7.5% Ni equivalent. The retention of austenite is due to the lower martensite formation starting (M_s) and finishing (M_f) temperatures; if the finishing temperature is below room temperature, the austenite will not completely transform to martensite. These temperatures change as a function of composition. The chemical composition of HCM12A and HT-9 are shown in Table 2.1 below.

Table 2.1. Elemental composition of HCM12A and HT-9 in wt.% in the as-received condition [5].

Element	HCM12A	HT-9
Cr	10.83	11.63
Mo	0.3	1
Mn	0.64	0.52
Ni	0.39	0.5
V	0.19	0.3
Cu	1.02	0.04
W	1.89	0.52
Si	0.27	0.22
Nb	0.054	–
C	0.11	0.2
N	0.063	0.047
Al	0.001	<0.01
P	0.016	0.02
S	0.002	0.006
Ti	–	0.002
O	–	0.013
Fe	Bal.	Bal.

Effects of Irradiation

Exposure to neutron radiation in a nuclear power plant tends to harden steel by introducing various types of defects. Three of the main types observed are dislocation loops, voids, and nanoclusters.

Dislocation loops

Loops are formed from a line of dislocations that have coalesced; often, a dislocation line in motion will encounter an obstacle and bend around it and rejoin itself, forming a loop around the obstacle. This process is known as the Orowan mechanism. The atomic displacements caused by radiation increase the irregularity of the lattice, forming dislocation loops. These loops themselves form an obstacle to dislocation motion, and thus they increase the hardness and strength of the alloy.
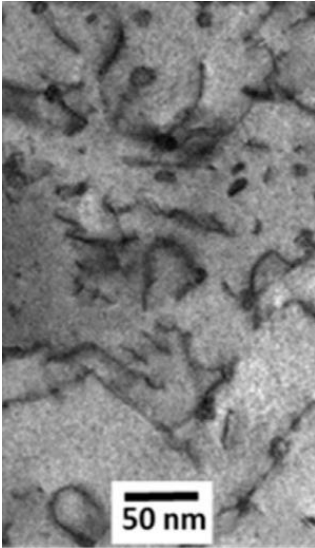
Figure 2.3. TEM image of loops in HCM12A [6].

Voids

The density of vacancies in the lattice is increased due to irradiation; as damage accumulates and more atoms are displaced, these vacancies can cluster and coalesce, forming larger voids in the lattice. These voids have been mainly observed after elevated-temperature irradiation [7]–[9]. Voids impede dislocation motion and harden the alloy. Additionally, due to the displaced atoms and higher amounts of vacant lattice sites and empty space in the matrix, the presence of voids causes swelling and dimensional stability issues [10].
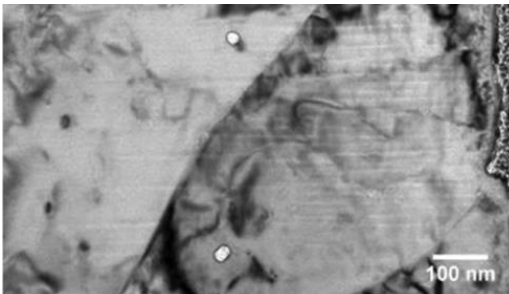
Figure 2.4. TEM image of voids in HCM12A [6].

Nanoclusters

Atomic displacements due to irradiation also cause solute cluster formation, in which alloying elements within the matrix migrate into the same area, forming a small region with a different composition than the surrounding material. Irradiation of high-Cr steel alloys causes nanoclusters of

several types [5], [11]. Higher dose rates of radiation tend to grow the nanoclusters and reduce their volumetric number density [5], [12].
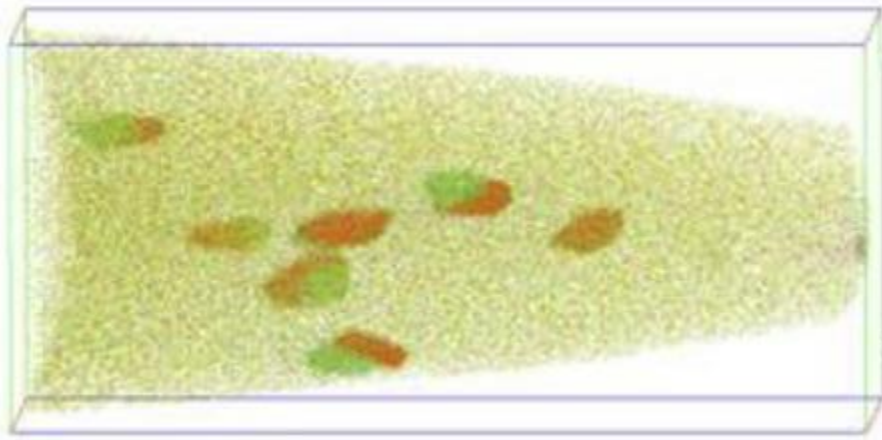
Figure 2.5. TEM image of nanoclusters in HCM12A [5]. The green clusters are Si-Mn-Ni and the red clusters are Cu.

Orowan Mechanism and Dispersed Barrier Hardening

Orowan Mechanism

The lattice defects described above influence the mechanical properties of the alloy. The mechanisms by which these features harden and strengthen the material depends on the type of obstacle. Precipitates can be either coherent with the matrix or incoherent. Coherent nanoclusters have a lattice structure that is aligned with the broader matrix of the grain in which it resides. Because of this, a coherent solute cluster does not form as strong an obstacle to dislocation motion. If coherent, a dislocation line may be able to shear through the particle; if incoherent, the dislocation line will move past the precipitate by bending around it in a process called the Orowan mechanism. In this process, described in [13] and [14], a dislocation line encounters an obstacle and is distorted by it. The line bends around the feature, surrounding it until it is transformed into an Orowan loop, as shown in the figure below, from [15].
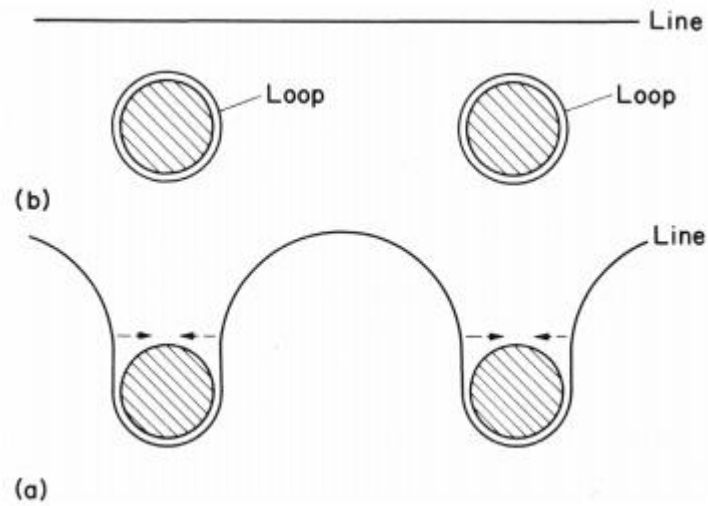
Figure 2.6. The Orowan mechanism. When an obstacle (nanocluster or precipitate) intercepts a moving dislocation line (a), the shear stress bends the line until it is surrounded, and the line forms a loop (b) [15].

The Orowan mechanism describes how the presence of nanoclusters and precipitates change the yield strength of the material. By forcing dislocation lines to either shear through or distort around them, these obstacles increase the stress required to move the dislocations. This effect is dependent on the type, size, strength, and density of the features.

Dispersed Barrier Hardening Model

The relationship between the size and number of obstacles in the matrix and the overall change in yield strength is typically described using the dispersed barrier hardening (DBH) model, which quantifies the shear stress required to move a dislocation line through an array of obstacles of a certain type and converts it to a change in uniaxial stress in terms of the obstacle size and density. The stress increment can be computed for each type of obstacle and the results superposed.

The hardness of a bulk metal alloy, and consequently its yield strength, is greatly affected by the material microstructure. Discontinuities of the crystalline lattice, precipitates or clusters of one or more alloying elements, and small voids or gas pockets all inhibit dislocation motion and thereby increase the strength of the lattice. The size of these nanofeatures and their number density per unit volume both influence how much the material's yield strength increases. The dispersed barrier hardening (DBH) model is a predictive equation that expresses a change in yield strength as a function of the average size and number density of each type of nanofeature. The DBH model is [10]:

$$\Delta\sigma_{y,i} = \alpha_i M \mu b \sqrt{d_i N_i} \qquad (1)$$

where M is the Taylor factor (equal to 3.06 for polycrystalline materials [16], [17]), μ is the shear modulus (82 GPa [18]), b is the Burger's vector (0.248 nm [19]), and d_i and N_i are the average diameter and number density of a given nanofeature type. The coefficient α_i represents the relative amount of strengthening that the specific feature type contributes to the alloy; a higher α indicates that the nanofeature type in question is a stronger barrier against dislocation motion, and a lower α indicates a barrier that is more easily passed. Values of α should be between 0 and 1 [20]. The strengthening factor may vary based on nanofeature type or radiation condition. The DBH equation is calculated for each barrier type, and the results are combined using linear or root-sum-square (RSS) superposition to predict the total increase in yield strength due to the nanofeatures. The constant material properties are shown in the table below.

Table 2.2. Material constants used in this study (all values are similar for HCM12A and HT-9).

	Shear modulus μ	Burger's vector b	Taylor factor M	Poisson's ratio ν
Value	82 (GPa)	0.248 (nm)	3.06	0.33
Source	[21]	[19]	[16], [17]	[22]

Nanoindentation

Rationale

Due to concerns of practicability and safety with respect to neutron irradiation, much irradiation-damage research is done using proton- or ion-irradiated samples [2], [3]. However, because of the interaction between the charged particles and the electrons in the metal sample, the distance of penetration and the depth of the damage peak during these tests is often very shallow, typically between 1 and 20 μm; the electron cloud in the metal resists the passage of ions and protons much more than neutrons. Because of this phenomenon, nanoindentation is the preferred method of investigating the mechanical properties such as modulus of elasticity and hardness. Conventional Vickers hardness testing or even micro-hardness testing deforms the sample below the level to which the radiation damage reaches, and thus includes an un-irradiated component into the force/displacement measurement. Furthermore, the plastic zone deformed by the penetration of the indenter is much greater than the depth of penetration; Dolph et al. estimate that the material sampled by the indenter is ~4-5 times the tip radius [23]. Therefore, the depth of penetration of the indenter

should be only 20-25% of the irradiation damage depth. The figure below is from Dolph et al [23], and depicts their study of irradiated ODS and the plastic zone surrounding the indenter tip.
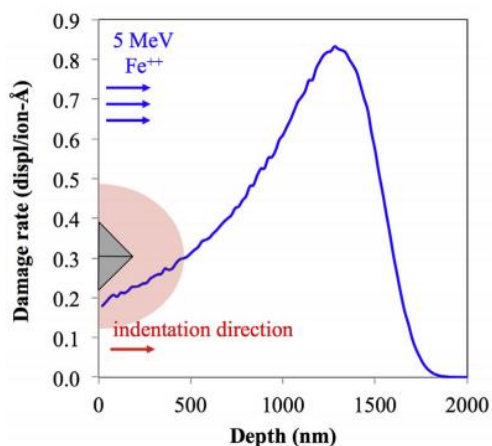
Figure 2.7. Diagram showing irradiation damage profile and plastic zone (not to scale) surrounding the indenter tip [23].

Methods

Two main approaches are used to find the modulus and hardness during a nanoindentation test: continuous stiffness measurement (CSM) and quasi-static stiffness measurement. In the CSM technique, the indenter tip is oscillated at a sufficiently high frequency (often 40Hz) to retrieve the force/displacement measurements continuously while progressively increasing the load to drive the tip into the material, giving a complete hardness vs. depth profile. This approach has the advantage of being able to continuously measure the hardness at every depth, rather than at a discrete set of points, giving a fuller picture of the material properties as a function of depth. There is evidence, however, that the oscillation of the tip in the material produces a change in the material itself; the alloy can strain-harden or soften under the variable load [24], [25]. With quasi-static testing, the indenter head penetrates and holds, then measures the elastic stiffness on retraction. This gives only discrete points at which the properties are known, but it avoids any issues arising from the application of a harmonic stress to the material. In this study, quasi-static nanoindentation was used rather than CSM.

Previous Studies

Potential structural or fuel cladding materials for nuclear power plants, and FeCr alloys specifically, have often been studied using ion irradiation and nanoindentation to simulate neutron damage. Kareer et al. [26] lists reasons for using charged particles as a surrogate for neutron

irradiation, including much lower levels of dangerous radiation, "cool-down" times several orders of magnitude shorter after radiation exposure and before becoming safely non-radioactive, and high amounts of irradiation-induced damage. The chief disadvantage is that the damage layer caused by charged particles is very shallow compared to neutron damage, and the damage profile is not consistent; thus, changes in the affected region can only be measured using specialized small-scale mechanical tests, and correcting the results to accommodate the variability in hardness throughout that small scale [26].

In their study of Fe-9%Cr ODS, Dolph et al. describe the indentation size effect, which affects shallow indentations and tends to increase the apparent hardness at shallow depths; they found the best range for the study of irradiation effects was at depths of $\gtrsim 200$ nm [23]. They also use an analytical method, a finite element model, and a nanoindentation and cross-sectional TEM experiment to quantify the size of the plastic zone surrounding an indenter tip. They conclude that the material sampled by the indenter is a hemisphere ~4-5 times the indenter tip penetration depth.

In their study of HCM12A, Allen et al. [27] show that proton and ion irradiations comparable to those in this study (including one using 2.0 MeV protons to 3 dpa at 500°C) cause increases in hardness mainly due to the formation of precipitate phases. Mechanical property changes were quantified using Vickers indentation, and microstructural changes were studied using TEM. Voids and loops were observed in several samples, particularly the ones irradiated at lower temperatures with protons; however, the study did not attempt to quantify the relative component changes in hardness due to loops as distinct from precipitates.

A general approach to finding the strengthening factors for dislocation loops, nanoclusters, voids, or α'-phase particles present in irradiated alloys using the DBH model and superposition is often used [28]–[30]. These studies investigate the effects of irradiation on the yield strength of a range of model Fe-Cr alloys due to defect clusters such as loops or precipitates. Porollo et al. [30] and Bergner et al. [28] use tensile testing to determine the change in yield strength. Porollo et al. used a four-feature approach (accounting for loops, voids, precipitates, and network dislocations), Bergner et al. used a three-feature approach (loops, nanoclusters, and α' particles) while Heintze et al. [29] used nanoindentation and a two-feature approach (loops and α' particles). Each of these studies assume that the solid solution strength is unaffected by irradiation.

In their study of Fe-9%Cr ODS steel, Swenson et al. [22] identify four component changes in yield strength: voids, dislocation loops, oxide nanoclusters, and solid solution strengthening. The

DBH model and linear and RSS superposition are employed, along with the results of nanohardness measurements, to identify values for each component strengthening factor α.

Results for strengthening factors found in these studies are shown in the table below.

Table 2.3. Summary of α-values for various alloys and nanofeatures as found by previous studies.

Source		Clusters	Loops	Voids	α'-phase Precipitates
Bergner	Linear	0.1	0.3	-	0.015
	RSS	0.134	0.44	-	0.03
Heintze	-	-	1.44	-	0.006
Porollo	-	-	0.68	0.17	0.85
Swenson	Linear	0.11-0.12	0.44	0.65	-
	RSS	0.05-0.06	-	-	-

Chapter 3: Experimental Methods

The purpose of this study is to correlate observed microstructural changes due to irradiation to changes in mechanical properties in two high-Cr alloys. The mechanical properties were measured using a nanoindentation technique.

HCM12A and HT-9 Sample Irradiation

The samples in this study comprise HCM12A and HT-9 in both the as-received and irradiated conditions. There were two types of irradiation done to each sample set; a 3 dpa irradiation using Fe^{2+} ions at 5 MeV, and a 2.4 dpa irradiation using protons at 2 MeV. Both irradiations were done at 500°C. These irradiations were carried out at the Michigan Ion Beam Laboratory; these experiments are described more fully in [5]; the diameter and number density data used in this study can be found in [5] (nanoclusters) and [6] (loops and voids). The damage profiles were estimated using the Stopping and Range of Ions in Matter (SRIM) software. The SRIM output is shown in the figure below.
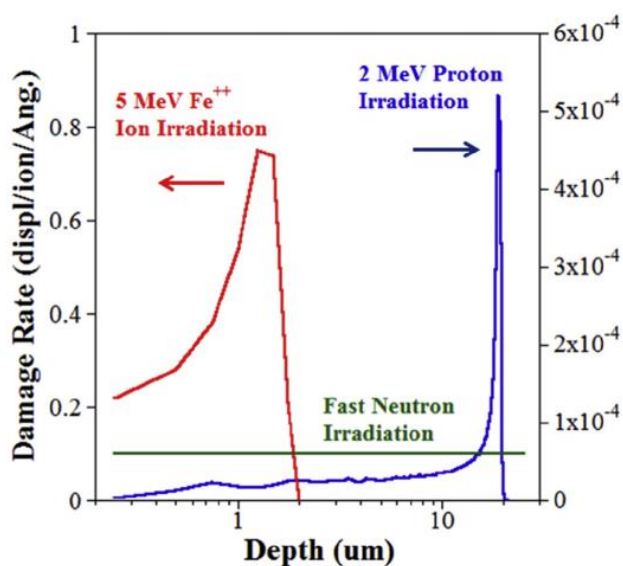
Figure 3.1. SRIM output estimating the level of damage as a function of depth into the surface, with neutron irradiation shown as a reference [5].

Note that in the proton case, an irradiation of 3 dpa in "Detailed Calculation" mode in SRIM equates to 2.4 dpa in "Quick Calculation (K-P)" mode. This is why the HCM12A proton-irradiated samples were exposed to 2.4 dpa rather than 3 dpa. The irradiated sample conditions are shown below with details from [6].

Table 3.1. Irradiation conditions and parameters for HCM12A and HT-9. All irradiations done at 500°C.

Alloys	Fe2+ irradiation $(2.2\times10^{-4}$ dpa/s)	Proton irradiation $(1.2\times10^{-5}$ dpa/s)
HCM12A	3 dpa,	2.4 dpa
HT-9	3 dpa	—

Nanoindentation

 Nanoindentation was conducted at KLA-Tencor in Milpitas, California. Samples were prepared for indentation by using epoxy adhere them to a glass bed which had been glued to an aluminum puck. A diagram and photo of the sample is shown below.
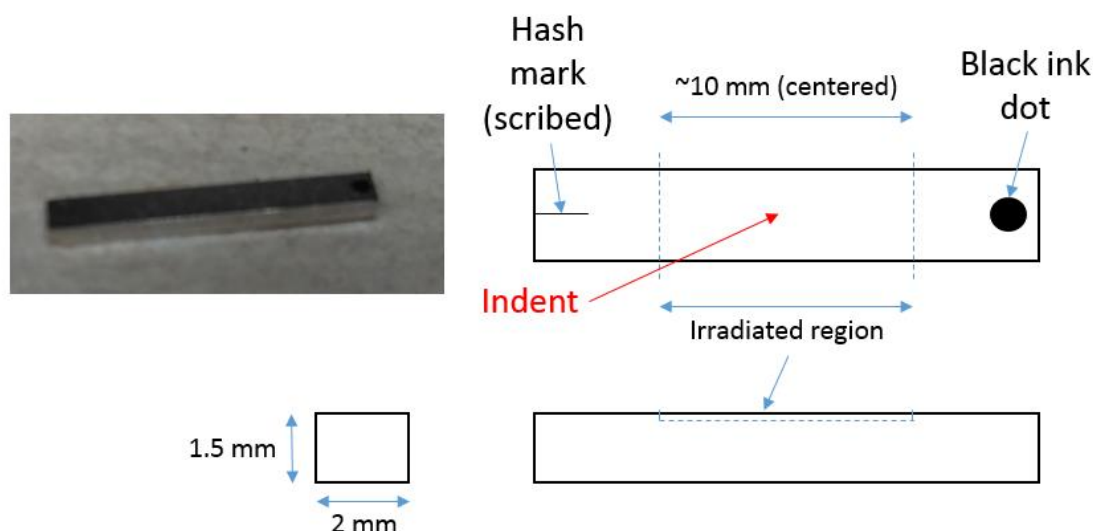
Figure 3.2. Diagram showing HCM12A irradiated sample; HT9 sample was similar but with two scribed hash marks on the end.

 Overview

 Because the heavy ion and proton irradiation causes damage to only a very shallow layer at the surface of the sample, any material property measurement technique must be able to quantify and record data at very small scales. Nanoindentation can record applied loads very precisely, and displacements at high spatial resolution; for this reason, it is often used to measure the changes in the surface of a material due to irradiation by charged particles.

 By applying a precisely known load to an indenter tip of known geometry and recording the subsequent displacement of the tip into the sample, the material properties of the sample such as

hardness and elastic modulus can be derived. Hardness is defined as the applied force divided by projected area of contact. The contact area can be described as a function of the indentation depth; this function depends on the tip geometry. The nanoindentation in this study was done using a Berkovich indenter tip. The Berkovich is a 3-sided pyramid, a shape that is much easier to shape to a single point than a four-sided shape, which can be difficult to manufacture without leaving an edge at the tip rather than a single point. (Geometrically, an ideal pyramid of three planes must meet at a point, whereas a pyramid of four planes must have each plane located precisely to form a point.)

Two sources of experimental error must be dealt with in nanoindentation. Ideally, a Berkovich indenter tip has an area function $A = 24.5{h_c}^2$ where A is the contact area and h_c is the contact depth [31]. However, the indenter tip can become worn or damaged with use, and the tip profile can lose sharpness or deviate from the ideal angle. Another issue that must be addressed is the flexibility of the indenter frame itself. Any compliance in the mechanism or the sample mount will show up in the displacement data. Frame compliance must be addressed if the data is to be useable.

Both the issue of the indenter tip geometry and the frame compliance can be corrected for by performing a tip calibration. In the calibration process, a standard sample of known modulus, usually fused silica, is indented a number of times to a full range of different depths. A polynomial curve fit is then found describing the contact area as a function of depth, such that, when applied to the force-displacement data from the calibration, the curve fit will closely reproduce the known modulus. When this convergence is achieved, the area function will account for deviations from the ideal from both a blunted indenter tip and frame flex/compliance. This process is known as the Oliver-Pharr method [32]. The unknown elastic modulus of a new material can then be determined by examining the force-displacement curve from a load-unload cycle of the nanoindenter and using the area function determined previously.

The loading phase creates both elastic and plastic deformation, whereas the unload phase will only create elastic deformation; this is similar to a standard tensile test. For this reason, mechanical properties are derived using the data from the unloading portion of the cycle. *Stiffness* is the change in load with respect to depth as the tip is withdrawn; it can be used to calculate the modulus using the area function. Similarly, *hardness* is defined as the maximum load divided by the contact area; it can be used to calculate the yield stress.

<u>Setup and Indentation Parameters</u>

The indentation method used in this study is called quasi-static. In the quasi-static method, the load is increased to drive the tip into the material and then fully withdrawn. When driving into the material, it is unknown how much of the displacement is elastic or how much is plastic; however, when withdrawn, all recovered displacement is assumed elastic. Thus the properties are measured upon retraction. This process is repeated; the indenter depth is increased incrementally, and the indenter must be fully withdrawn to measure properties at different depths.

In this study, the indentations were made using a G200 nanoindentation testing machine from KLA and the Dynamic Contact Module (DCM) head. A surface detection threshold stiffness of 200 N/m was used; this parameter is used to identify when the tip contacts the sample surface. If this threshold is set too low, signal noise may cause it to identify surface contact too early, and if set too high, the tip will indent the surface before data collection begins. In either case, the displacement will be misreported and the modulus and hardness data may be skewed. Tip calibration was done using a sample of fused silica as a standard; a 2nd-order polynomial area function was fitted, and analysis was done in the NanoSuite software using the Oliver-Pharr method.

The tests were load-controlled rather than displacement-controlled. In a load-controlled test, the maximum load is set by the user, rather than the maximum depth. The DCM head can apply a maximum load of 30 mN; the average load required to achieve an indentation depth of 600 nm in as-received HT-9 was about 25 mN; in irradiated HT-9 the required load was about 26.5 mN. (These values were determined from preliminary CSM tests conducted to obtain an estimate of the load-depth curves.) The maximum loads for these tests were 2.5 grams-force, or 24.5 mN.

The indentations were made into the irradiated surface using the G200 instrument and the "Basic Method". Each sample was indented at fifteen different locations, spaced at least 60 μm apart to avoid plastic zone interference. The tip was loaded and unloaded at twenty depths per indent site, with progressively more unloadings at greater depths. This was to ensure that there was a sufficient resolution of data in the 200-400 nm range. Each indentation load cycle included a 15-second load time and a 10-second hold at maximum load, followed by a 90% unload. The load-displacement curve for a single indentation site is shown below.
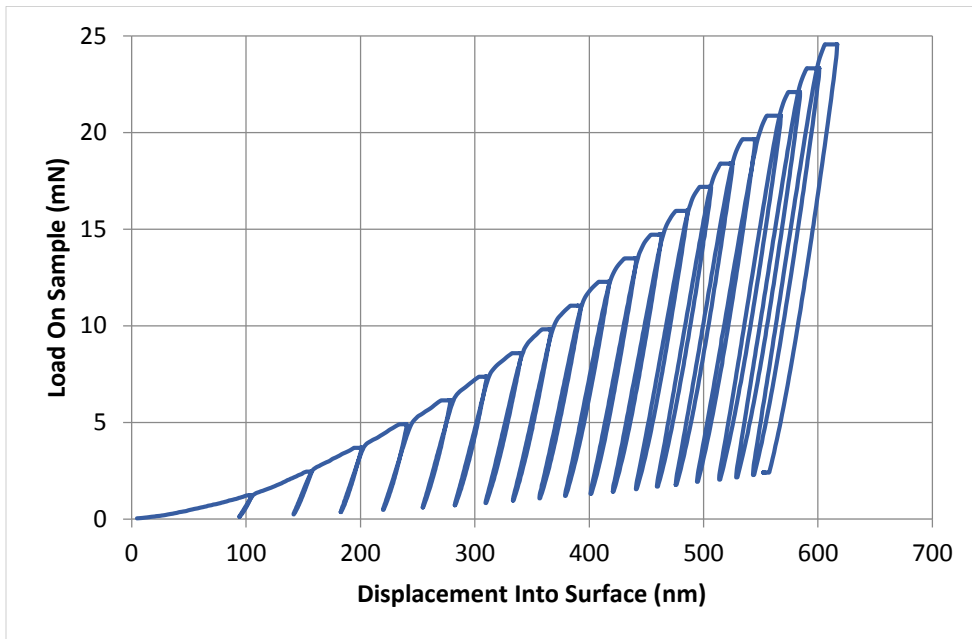
Figure 3.3. Plot of the load-displacement curve in HCM12A for a single indentation location. Note the creep during the 10-second hold time at each load peak, the increasing frequency of unloads at greater depths, and the 90% unloads.

A similar method was used for the HCM12A and the HT-9. Note in Figure 3.1 that the damage peak from proton irradiation is located much deeper the ion damage. Consistent indentation techniques and depths were used to control the experiment, for all samples and irradiation conditions for both alloys.

Chapter 4: Results

Reduction of Hardness Data

The nanoindentation data for the alloys and irradiation conditions in this study includes measurements of hardness from the surface down to about 650 nm deep. The samples were indented at a number of sites under load control, and hardness was measured at a number of depths per indentation site. This information is summarized in the table below.

Table 4.1. Number of hardness testing locations and depths per alloy and irradiation condition.

Alloy	Radiation Condition	Number of Locations	Number of Depths
HCM12A	As Received	16	14
	Heavy-ion Irradiated	15	14
	Proton Irradiated	14	19
HT-9	As Received	15	19
	Heavy-ion Irradiated	15	19

To reduce this data to a single change in hardness value for each irradiation condition, two computations were carried out. First, the average depth for each incremental hardness measurement was computed. For example, for the as-received HCM12A, hardness was measured at 14 different depths per location, but because the tests were load-controlled, there is some variation in the depths at which hardness is known. Second, the average hardness was computed at each incremental measurement; even though the tests were load-controlled, there was some variation in measured hardness. (Ideally, for instance, the first measurement at each location should have reported the same load but slightly different depths, and so for the second measurement etc. But due to small inconsistencies in the load control, there is some small variation in the incremental loads measured at each depth.) These two averages reduced the data set to 14 depth-hardness pairs. The hardness-displacement measurements for the as-received HCM12A are shown in the figure below. Finally, all combined averages at depths less than 200 nm or greater than 400 nm were eliminated, and the remaining points were averaged to a single hardness value. This single value was used in all subsequent computations.
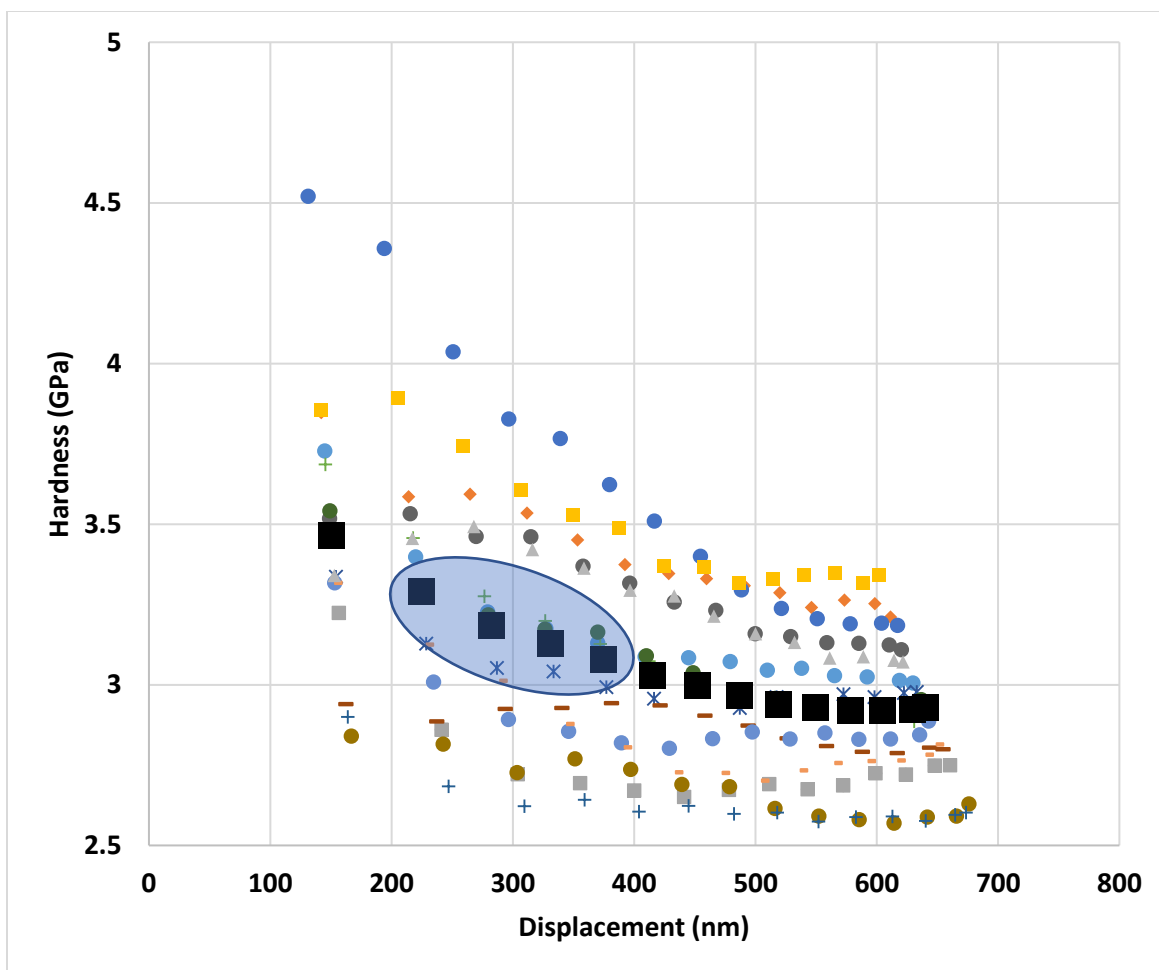
Figure 4.1. Hardness vs. depth for as-received HCM12A. Each series represents hardness measurements at a unique indentation location. The large squares represent the average hardness measurement for each average depth increment. The oval shows the values that fall within the region analyzed by this study.

The depth range of interest was selected by necessity. First, given that the plastic zone size is 4 to 5 times the indentation depth, a depth of 400 nm effects a region up to 2000nm deep, which is the approximate limit of the irradiation-damaged region of the material. It is undesirable to include any sampling of the hardness of the unaffected zone; thus, any indenter data from deeper than 400 nm is likely skewed. Second, the small indentation size effect and other surface effects change the shallowest data in ways that are difficult to predict; for this reason, 200 nm was selected as the minimum depth for data included in the analysis.

Hardness and Yield Strength

A distinction must be made between the hardness as measured by nanoindentation and the yield strength as is often measured using a tensile test. The micro- or nanohardness is not identical to

the yield strength; however, it is directly proportional, and the relationship has been studied for ferritic steels [17]. There is a constant factor of 94.5 to convert from the Berkovich hardness in GPa to Vickers hardness in kg$_f$/mm^2 [33], and a factor of 3.06 that relates Vickers hardness to yield stress in MPa for ferritic steels [17]. Thus, the equations for obtaining yield stress from nanoindentation data are

$$HV = 94.5H \tag{2}$$

$$\Delta\sigma_y = 3.06\Delta HV \tag{3}$$

where *HV* is Vickers hardness and *H* is the measured Berkovich hardness.

Overview of Data

In both alloys, several trends are recognized. In general, both hardness and the amount of scatter in the hardness measurements decreases with increasing depth. The first of these effects can be partly attributed to the indentation size effect, which cannot be ignored at these shallow depths. The challenge is to avoid both the shallowest material, where the size effect is most disruptive, and the unirradiated material below the surface, given the consideration that the tip samples 4-5 times deeper than the indentation depth. Aydogan et al. [7] and Heintze [29] describe this challenge, and explain that the decreasing hardness with increasing depth is due to the size effect increasing the hardness toward the surface, irrespective of other microstructural effects including irradiation damage. Similarly, the scatter at shallower depths is likely due to imperfections in the surface or it can be attributed to the indentation size effect as well.

The hardening of the two alloys is presented in the figures below.
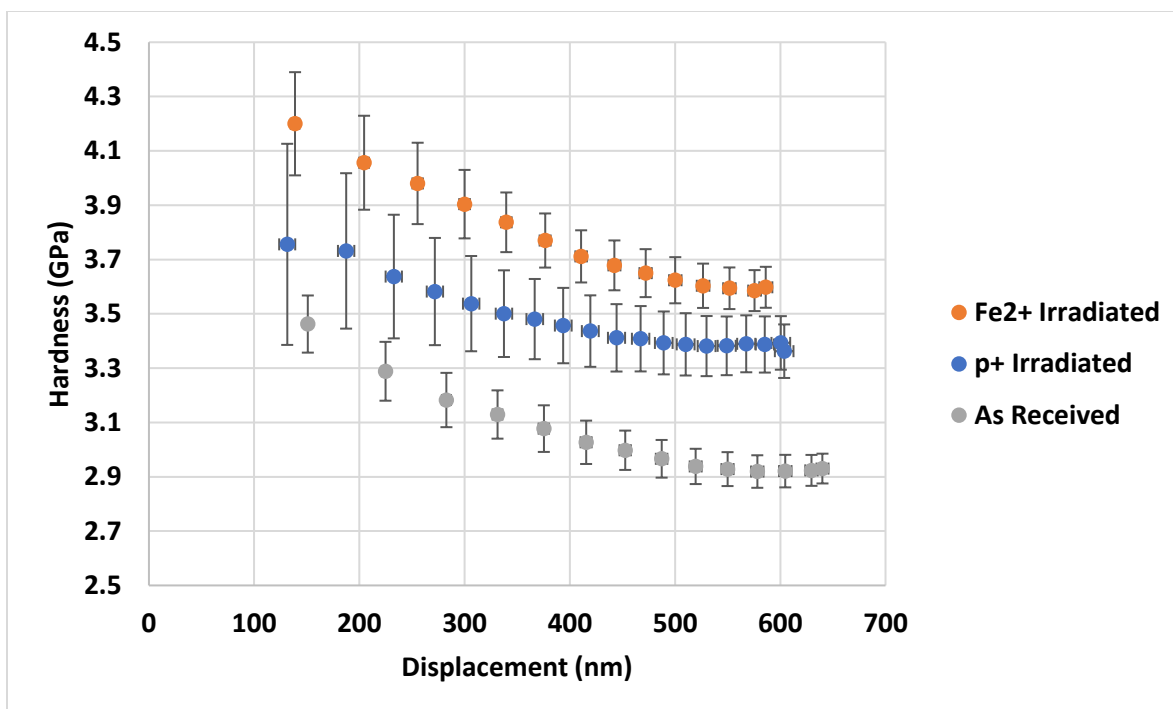
Figure 4.2. Hardness vs depth for HCM12A. The error bars (horizontal and vertical) represent the standard deviation of the mean, or $S/\sqrt{N}$ where S is standard deviation and N is number of samples.
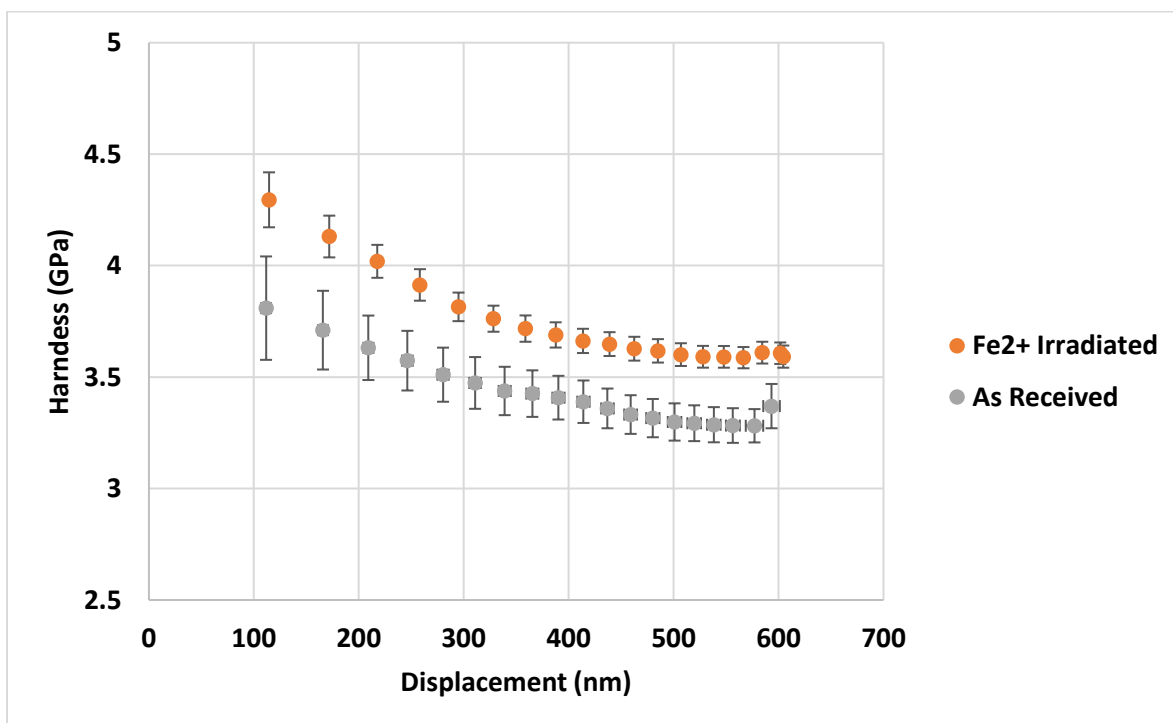
Figure 4.3. Hardness vs depth for HT-9.

The total change in hardness from the as-received to irradiated conditions for each alloy is determined according to the process described in the previous section. These results are shown in the table below.

Table 4.2. Average measured hardness values for HCM12A and HT-9, 200 nm to 400 nm. All values in GPa.

	As-received	Fe^{2+}-irradiated	Proton-irradiated
HCM12A	3.17	3.91	3.53
ΔH	-	**0.74**	**0.36**
HT-9	3.49	3.82	-
ΔH	-	**0.32**	-

These values are in line with published results. Allen et al. [27] note an increase of 0.15 GPa in HCM12A when irradiated with protons to 3 dpa at 500°C, and 0.49 GPa when irradiated to 10 dpa at 400°C. Wharry et al. [34] describe an increase in hardness in T91 (a similar F-M steel) of 0.239 GPa after a 3 dpa proton irradiation dose at 400°C. Krumwiede et al. [35] found that after an exposure of 6.49 dpa at 320°C, alloy T91 hardened by 0.99 GPa, and HT-9 hardened by 1.45 GPa. Gao et al. [19] found the hardening of reduced activation martensitic steel F82H under Fe^{3+} irradiation to 30 dpa at 300°C to be 0.85 GPa. Zeman et al. [1] reports a hardening in T91 under 3.5 dpa proton irradiation (120°C) of about 0.116 GPa. Zhang et al. [36] observed an increase of about 0.163 GPa in a 9Cr-2W steel alloy, and 0.217 GPa in a similar alloy with the addition of 0.1 wt% Si after a 0.1 dpa neutron irradiation.

Chapter 5: Discussion and Analysis

Introduction

The dispersed barrier hardening model predicts a component change in yield stress due to a single type of damage feature. Because two types of damage features were present in the HCM12A as well as solid solution hardening, there were more unknown variables than equations available to solve for the individual hardening components. The solid solution hardening was computed but there were still two damage feature types and only a single equation relating them to the total hardening. The HT-9, however, showed no clustering and therefore no change in solid solution composition either, so the total change in hardness was only due to dislocation loops, and the strengthening factor was readily solved for using the DBH model. Next, using the assumption that the dislocation core radius for loops in HT-9 will be the same as that for those in HCM12A, the strengthening factor for loops in HCM12A was calculated, and finally the factor for the nanoclusters as well.

Solid Solution Hardening Analysis

The compositional makeup within the matrix of each of the alloys in this study was changed as a result of the high temperatures and radiation exposure. This change in composition was brought about due to the formation of nanoclusters. The conditions of the experiment caused some of the solutes to precipitate out of solution and form these nanoclusters, thus changing the concentration of certain alloying solutes significantly—notably silicon, manganese, nickel, and copper. Because of the diminishing of these alloying elements, the yield strength of the matrix was lowered. When interstitial or substitutionary atoms are present in the lattice, they obstruct dislocation motion, increasing the yield strength. When, due to temperature and irradiation, some of these atoms are extracted from the lattice and formed into clusters, the BCC iron matrix is somewhat purified and the strength of the bulk lattice is reduced. The total increase in strength due to the presence of alloying elements can be modeled with a simple equation. The general solid solution strengthening model for BCC Fe-based alloys is [37]:

$$\Delta\sigma_{ss,i} = K_i C_i \qquad (4)$$

where $\Delta\sigma_{ss,i}$ is the component of solid solution strengthening due to the presence of each solute, K_i is the strengthening coefficient of each alloying element (MPa), and C_i is the atomic percent

composition (at%). The component strengthening can be calculated for each alloying element, and then summed to compute the total solid solution strengthening [37]:

$$\Delta\sigma_{ss} = \sum_i \Delta\sigma_{ss,i} \qquad (5)$$

Using these two equations, the change in solid solution strength due to irradiation can be computed. This solid solution data has not been published, but it was obtained as a result of the study by Swenson and Wharry on nanocluster irradiation evolution using atom probe tomography (APT) [5]. These values are shown in Table 5.1:

Table 5.1. Solid solution hardening in HCM12A due to changes in matrix composition, computed using equations (4) and (5). Sources are [37] and [38]; values used are approximations of values in sources.

Element	K_i (MPa)	As-received		Fe^{2+}-irradiated (3 dpa, 500°C)		Proton-irradiated (3 dpa, 500°C)	
		C_i (at%)	$\Delta\sigma_{ss,i}$ (MPa)	C_i (at%)	$\Delta\sigma_{ss,i}$ (MPa)	C_i (at%)	$\Delta\sigma_{ss,i}$ (MPa)
Si	30	0.60%	17.9	0.55%	16.5	0.48%	14.4
Mn	20	0.53%	10.6	0.67%	13.5	0.62%	12.4
Ni	20	0.99%	19.8	0.21%	4.1	0.13%	2.6
Cu	20	1.32%	26.3	0.21%	4.2	0.16%	3.2
Total			74.5		38.3		32.6
Change					**-36.2**		**-41.9**

These computed changes in yield strength due to solid solution hardening were used in conjunction with the dispersed barrier hardening model to give a more complete picture of the change in hardness (and therefore yield strength) than either model is capable of alone.

Microstructural Characterization and Dispersed Barrier Hardening

This study considers two types of irradiation-induced damage features—dislocation loops and nanoclusters—as well as solid solution hardening. None of the samples in this study contained any evidence of voids, so there is no net contribution to the increased hardness due to voids. Loops and nanoclusters were present in the irradiated HCM12A; only loops were present in the irradiated HT-9.

For both the HCM12A and HT-9, this study uses data obtained by Swenson and Wharry [5]. The microstructural characterization of the nanoclusters was conducted using APT. The results of

that study include volume fraction, number density, diameter, and nanocluster species information under a range of irradiation conditions. This information is summarized in the table below.

Table 5.2. Microstructural data for irradiated HCM12A and HT-9. Neither clusters nor loops were observed in either alloy in the as-received condition.

| | HCM12A: | | | | HT-9 | |
| | Fe^{2+} | | p$^+$ | | Fe^{2+} | |
	d (nm)	N (10^{-6} nm^{-3})	d (nm)	N (10^{-6} nm^{-3})	d (nm)	N (10^{-6} nm^{-3})
Si-clusters	5.95	92	9.63	19	-	-
Cu-clusters	6.18	107	6.82	19	-	-
Combined	7.44	107	10.66	19	-	-
Loops	7.67	2.20	7.6	4.4	7.6	2.00

In the HCM12A, two types of clusters are observed; Si-Mn-Ni-rich clusters and Cu-rich clusters. The APT images show that very often, the Cu-rich nanoclusters are located adjacent to the Si-rich clusters. This phenomenon has also been observed by Jiao and Was [39] in HCM12A. Swenson and Wharry suggest that the Cu-rich clusters precipitate at a lower radiation level, and the Si-Mn-Ni-rich clusters form at or near the surface of the Cu clusters.

To account for this tendency of the nanoclusters to appear in pairs, three alternative approaches were taken to represent the diameter and number density of the nanoclusters in this analysis. The first approach was to represent the two types of nanoclusters distinctly; that is, in the computation of the DBH model, the two types of nanoclusters would each have their own unique strengthening coefficient, and the diameters and number densities of each cluster type would be used, disregarding the tendency for the two types to be co-located. There are two drawbacks to this approach; it generates two unknown strengthening factors that must be solved for, and it neglects the fact that the two nanoclusters may interact with the matrix as one, due to their proximity/contact. The second approach was a simple sum of all the nanoclusters, treating the two types as similar, with no distinction being made between them for purposes of the DBH model. The effective particle diameter was calculated as a simple weighted average, and the number density was the sum of the densities of each type. This approach had the advantage of requiring only a single α-value to model the hardening, but it ignored both the distinction between the particle types and any effects due to their frequent proximity or co-location. The third approach, used throughout this study, combines adjacent nanoclusters into a larger one of the same volume. In the heavy ion-irradiated condition, there were more Cu-rich clusters than Si-rich clusters observed, so it was assumed that each Si cluster was paired

with a Cu cluster, and from this, the combined volume was computed, and the effective diameter calculated was from the volume. Finally, a weighted average of the combined cluster diameter and the remaining, unpaired Cu cluster diameter was computed; this weighted average was taken to be the effective cluster diameter. The number density was taken to be equal to number density of the Cu-rich clusters, again observing that each Si-rich cluster was paired with a Cu-rich cluster, leaving some Cu-rich clusters unpaired. The nanocluster data for the HCM12A was published by Swenson et al. [5] and is shown in the table above. (No nanoclusters were observed in either the as-received or irradiated HT-9 samples.) The characterization of the loops was conducted using transmission electron microscopy (TEM) [6].

Solutions for Strengthening Factors

The following sections describe four mathematical approaches to identifying the DBH constants from the hardness data. The first is a direct approach solving for the strengthening factors from the measured changes in hardness. The second and third use a closed-form equation for the strengthening factors for incoherent clusters. The fourth uses a solution derived from the HT-9 data to simplify the equation system used for the HCM12A data.

Approach 1

This study began by attempting to solve for the strengthening factors directly using the measured changes in hardness. This approach uses the DBH model, in conjunction with linear and RSS superposition, to simultaneously solve for all strengthening factors and component changes in yield strength. The DBH equation system is shown below:

$$\Delta\sigma_{NC}^{Fe^{2+}} = \alpha_{NC}M\mu b\sqrt{N_{NC}^{Fe^{2+}}d_{NC}^{Fe^{2+}}} \tag{6}$$

$$\Delta\sigma_{loops}^{Fe^{2+}} = \alpha_{loops}M\mu b\sqrt{N_{loops}^{Fe^{2+}}d_{loops}^{Fe^{2+}}} \tag{7}$$

$$\Delta\sigma_{NC}^{p^+} = \alpha_{NC}M\mu b\sqrt{N_{NC}^{p^+}d_{NC}^{p^+}} \tag{8}$$

$$\Delta\sigma_{loops}^{p^+} = \alpha_{loops}M\mu b\sqrt{N_{loops}^{p^+}d_{loops}^{p^+}} \tag{9}$$

In the above four DBH equations, the alpha values for loops and nanoclusters are unknown but assumed constant across radiation conditions; that is, it assumes the strengthening factor for nanoclusters in HCM12A is the same in the ion-irradiated sample as in the proton-irradiated sample, and similarly for the strengthening factor for loops. The component changes in hardness are unknown as well. To solve for these six unknowns, superposition is used to match the component changes in hardness to the measured total change for each condition. The two equations below use linear superposition to provide the two final equations, and the system of six equations can be solved simultaneously for the four component changes in yield strength and the two strengthening factors:

$$\Delta\sigma_{measured}^{Fe^{2+}} = \Delta\sigma_{NC}^{Fe^{2+}} + \Delta\sigma_{loops}^{Fe^{2+}} + \Delta\sigma_{SS}^{Fe^{2+}} \tag{10}$$

$$\Delta\sigma_{measured}^{p^+} = \Delta\sigma_{NC}^{p^+} + \Delta\sigma_{loops}^{p^+} + \Delta\sigma_{SS}^{p^+} \tag{11}$$

The two equations below use RSS superposition instead of linear; again, this gives a system of six equations and six unknowns.

$$\Delta\sigma_{measured}^{Fe^{2+}} = \sqrt{\Delta\sigma_{NC}^{Fe^{2+}2} + \Delta\sigma_{loops}^{Fe^{2+}2}} + \Delta\sigma_{SS} \tag{12}$$

$$\Delta\sigma_{RSS}^{p^+} = \sqrt{\Delta\sigma_{NC}^{p^+2} + \Delta\sigma_{loops}^{p^+2}} + \Delta\sigma_{SS} \tag{13}$$

The results of this approach, using both the linear and RSS superposition methods, are summarized in Table 5.4 below:

Table 5.3. Approach 1, direct simultaneous solution for strengthening factors for loops and nanoclusters in HCM12A using linear and RSS superposition.

	α_{loops}	α_{NC}
Linear	-0.178	0.177
RSS	±0.288i	±0.157

Strengthening factors must be real values between 0 and 1 [20]. This result indicates that this first approach contains one or more incorrect assumptions about the nature of the nanofeatures in the

alloy, probably the assumption in this method that the strengthening factor for a given feature type is constant regardless of irradiation condition or nanofeature size and density. However, it is not possible to use this method without that assumption, because there are only four DBH equations and two superposition equations available. The four component changes in hardness are unknown; the system could not be solved with any more than two unknown strengthening factors. A graphical summary of this approach is shown below.

Dispersed Barrier
Hardening

$\Delta\sigma_{NC}^{Fe^{2+}}$

Closed-form
equations

$\Delta\sigma_{measured}^{Fe^{2+}}$

$\Delta\sigma_{loops}^{Fe^{2+}}$

Solve for
α's

$\Delta\sigma_{NC}^{p^+}$

$\Delta\sigma_{measured}^{p^+}$

$\Delta\sigma_{loops}^{p^+}$
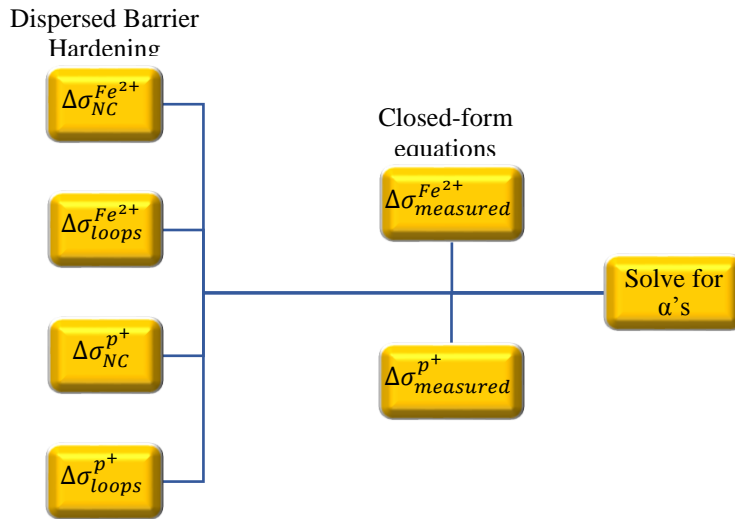
Figure 5.1. DBH equations model the component changes in yield stress with all α's unknown; these expressions are then substituted into the superposition equations and set equal to the measured changes in strength to solve for the α's simultaneously.

Approach 2

The second approach used to find strengthening factors was based on the work of Tan and Busby [13], who offer closed-form equations to predict the barrier strengths for various precipitate shapes based on their size, density, and other factors. Incoherent precipitates offer a higher resistance to dislocation motion due to the Orowan dislocation bowing mechanism, whereas coherent particles can shear more readily and allow dislocations to pass through. For spherically-shaped incoherent precipitates, the model is:

$$\alpha_{nc}^{incoh} = \frac{0.135}{(1-v)^{1/2}\left(1-0.816d\sqrt{Nd}\right)}\ln\left(\frac{0.816d}{r_0}\right) \tag{14}$$

where α_{nc}^{incoh} is the incoherent nanocluster barrier strength, v is Poisson's ratio, d is the particle diameter, N is the particle number density, and r_0 is the dislocation core radius.

They also provide a model to compute the value of α for dislocation loops based on the diameter, number density, and dislocation core radius:

$$\alpha_{loops} = \frac{0.271A}{(1-v)^{1/2}\sqrt{Nd}(16-\pi tA)} \ln\left(\frac{0.637d}{r_0}\right) \tag{15}$$

where t is the loop thickness (0.165 nm [22]), and $A = \sqrt{16\pi Nd} + 4Nd^2 - \pi^2 Ndt$. Using these two equations, an approximation of the strengthening factors can be obtained. The value of the dislocation core radii can be first-order approximated as being equal to the Burger's vector. With this assumption, the predicted values of α_{nc}^{incoh} are 0.63 and 0.67 for the Fe^{2+}-irradiated and proton-irradiated conditions, respectively. These values, when substituted into the DBH model equations, predict $\Delta\sigma_{nc}$ values of 1117 and 592 MPa—much higher than the total hardening observed in the samples. This second approach makes two assumptions, both of which are most likely false: it assumes the nanoclusters are incoherent, and it assumes that the dislocation core radii for both loops and nanoclusters are equal to b, the lattice parameter.

The graphical summary of this approach is shown below.
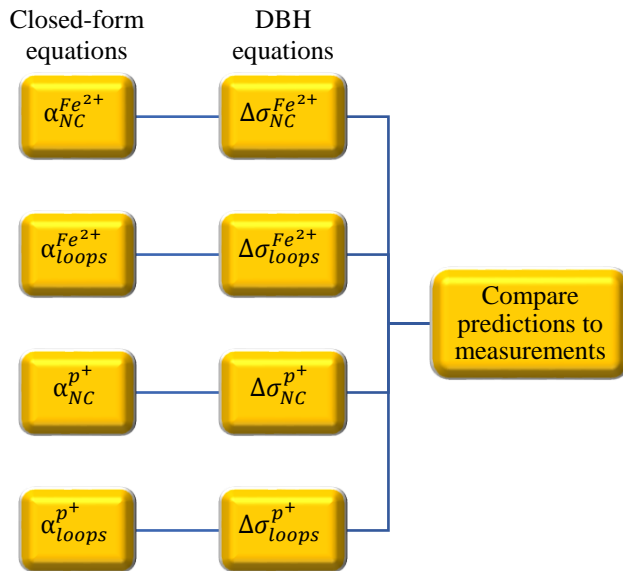
Figure 5.2. Closed-form equations are used to compute α directly from d and N. The α values are then used in the DBH model to predict the component changes as well as total change in material hardness.

Approach 3

A third approach was used to address the issue of the unknown dislocation core radii. To obtain a more accurate value of r_0, the closed-form equation for α_{nc}^{incoh} is rearranged, simplified, and plotted for similar samples available in the literature. A similar approach is used to find r_0 for loops. The data used for this approach is from Swenson and Wharry [5], and is shown in Table 5.5:

Table 5.4. Diameters and densities of nanofeatures in HCM12A and HT-9.

Alloy	Irradiation Condition	Si-Mn-Ni Clusters		Cu Clusters		Dislocation loops	
		d (nm)	N ($\times 10^{-6}$ nm^{-3})	d	N	d	N
HCM12A	Fe^{2+}, 3 dpa, 500C	5.95	92	6.18	107	7.67	2.2
	Protons, 2.4 dpa, 500C	9.63	19	6.82	19	7.60	4.4
	Neutrons, 3 dpa, 500C	4.36	398	4.59	372	7.50	4
HT9	Protons, 2.4 dpa, 500C	7.47	29	0	0	7.47	2.4
	Neutrons, 3 dpa, 500C	5.09	404	0	0	7.56	2.4

From this diameter and number density data, the value of the strengthening factor was computed using the closed-form equation for spherical incoherent particles or loops respectively, first setting $r_0 = b$. These alpha values were then plotted against the particle diameters. A least-squares curve of the form $\alpha = k_1 \ln(k_2 d)$ can be easily derived from the closed-form equation for both incoherent nanoclusters and loops, according to method described in ref. [27]. The parameters of the fit are then used to solve for r_0; from equation 12, it is seen that $r_0 = 0.816/k_2$ for incoherent nanoclusters, and from equation 13, $r_0 = 0.637/k_2$ for loops. These plots are shown below:
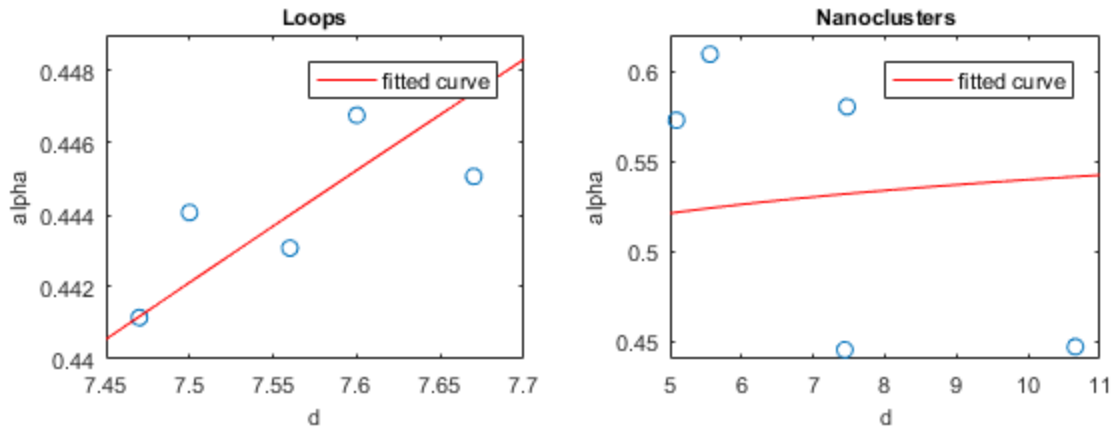
Figure 5.3. Plots showing the relationship of predicted strengthening factors versus nanofeature diameter for HCM12A and HT-9 under several irradiation conditions, shown with curve fits. *d* is in nm.

These curve fits give values of r_0 for loops as 0.218 nm, equal to 88% of the Burger's vector, but for nanoclusters as 0.000 nm. Ultimately, the results of this approach proved less than useful. The reason for the failure of this method to give reasonable results for the r_0 value for incoherent nanoclusters is because the closed-form equation predicts a higher strengthening factor for larger particle diameters; as seen in the figure above, however, the data used in this study generally has lower predicted alpha values for larger particle diameters. This indicates that the particles are likely coherent, and therefore cannot be modeled using the incoherent particle equation. The results of these curve fits are shown in the table below.

Table 5.5. Fitted solutions for dislocation core radii in HCM12A and HT-9. (Lower and upper 95% confidence bounds in parentheses.)

	k1	k2	Predicted r0 value (nm)
Loops	0.144 (-0.113, 0.400)	2.92 (-13.2, 19.0)	0.2184
Nanoclusters	0.0269 (-0.508, 0.561)	5.26×10^7 (-2.06×10^{10}, 2.07×10^{10})	1.5519×10^{-8}

A graphical summary of this approach is shown below.
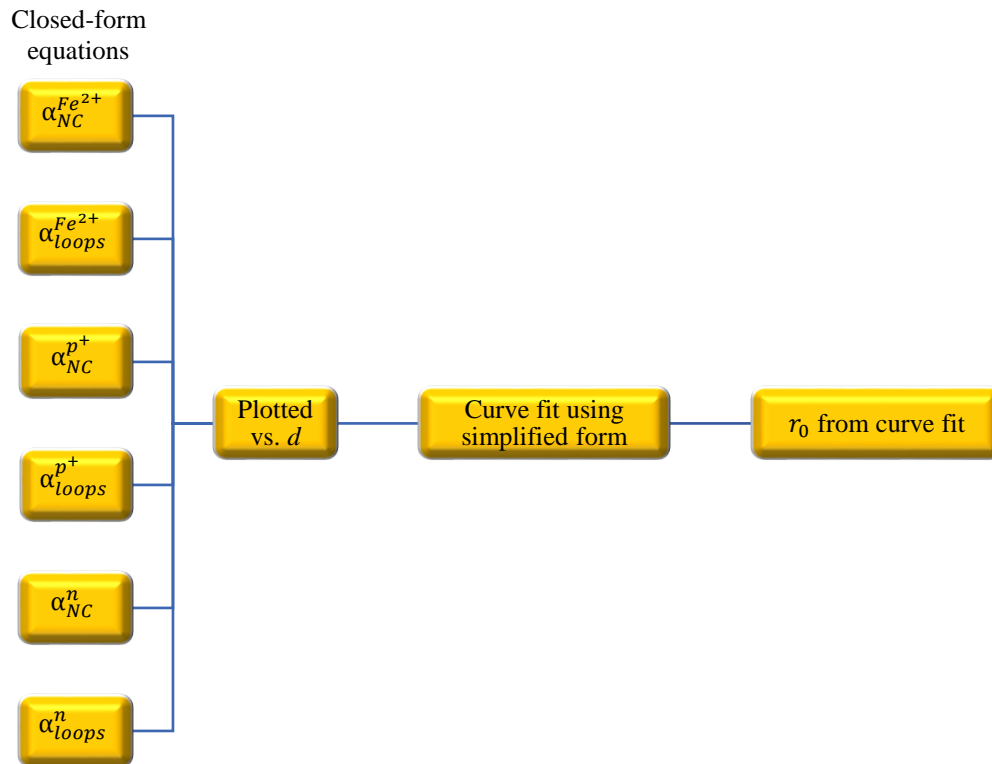
Figure 5.4. Closed-form equations are used to predict α's; these are then plotted vs. nanofeature diameter, and a curve in a simplified form of the predictive equation is used to extract r_0.

Approach 4

This approach involved taking advantage of the fact that the HT-9 samples had a simpler microstructure to reduce the number of unknown variables in the equation system. The as-received HT-9 sample included no loops, voids, or nanoclusters, and the Fe^{2+}-irradiated sample included only loops. Because there was no clustering, the solute concentrations were unchanged and solid solution hardening could therefore be neglected as well. Furthermore, because there was only one type of damage feature present to attribute the change in hardness, the value of α for the loops was easily solved for using the DBH model. The measured change in hardening between the as-received and the irradiated HT-9 produced a change in yield strength of 93.9 MPa, an increase due only to the formation of loops. The average diameter was 7.6 nm, and the average number density was 2.0×10^{21} m^{-3}. Using this data, the DBH equation was solved for the strengthening factor, which was found to be α = 0.387. This value is in line with published information [19], [28], [40].

From the closed-form equation for the strengthening factor of dislocation loops from Tan and Busby (equation 13), the value of the dislocation core radii r_0 for loops was obtained. The inputs were the computed value of α for loops and the size and number density for HT-9; the output was a value of r_0 for loops useable for both HT-9 and HCM12A. To obtain α for loops in HCM12A, the dislocation core radii was taken as constant between the two alloys. Using the number densities and loop diameters from the HCM12A and the value of r_0 obtained from the HT-9, the same equation was then solved for the HCM12A α_{loops}. Finally, having obtained α_{loops} from the HT-9 sample, the number of unknowns in the combined yield strength equations (for both linear and RSS superposition) was reduced to one. A straightforward solution for α_{nc} was now possible. A flowchart of this analysis is shown in Figure 5.2.

The results of both the linear and RSS equations are shown in the table below. In the first category (HT-9 loops), the Δσ value was measured and the α and r_0 values were calculated from the DBH model. In the second category (HCM12A loops), the Δσ values were calculated using the closed-form loop equation and the r_0 value found from HT-9, and the α values were found from the DBH model. In the third category (HCM12A nanoclusters), the Δσ values were found by using the measured total hardening, the calculated SS hardening, the Δσ values from the loops, and the superposition equations; the α values were found from the DBH model.

Table 5.6. Approach 4 solutions for strengthening factors in HCM12-A and HT-9; r_0 was found to be 0.360 nm.

	HT-9 Loops	HCM12A Loops		HCM12A Nanoclusters			
	Fe^{2+}	Fe^{2+}	p^+	Fe^{2+}		p^+	
	irradiated	irradiated	irradiated	irradiated		irradiated	
				Linear	RSS	Linear	RSS
α	0.387	0.389	0.390	0.0857	0.131	0.0073	0.0489
$\Delta\sigma$ (MPa)	94.0	99.5	141	150	229	6.49	43.2
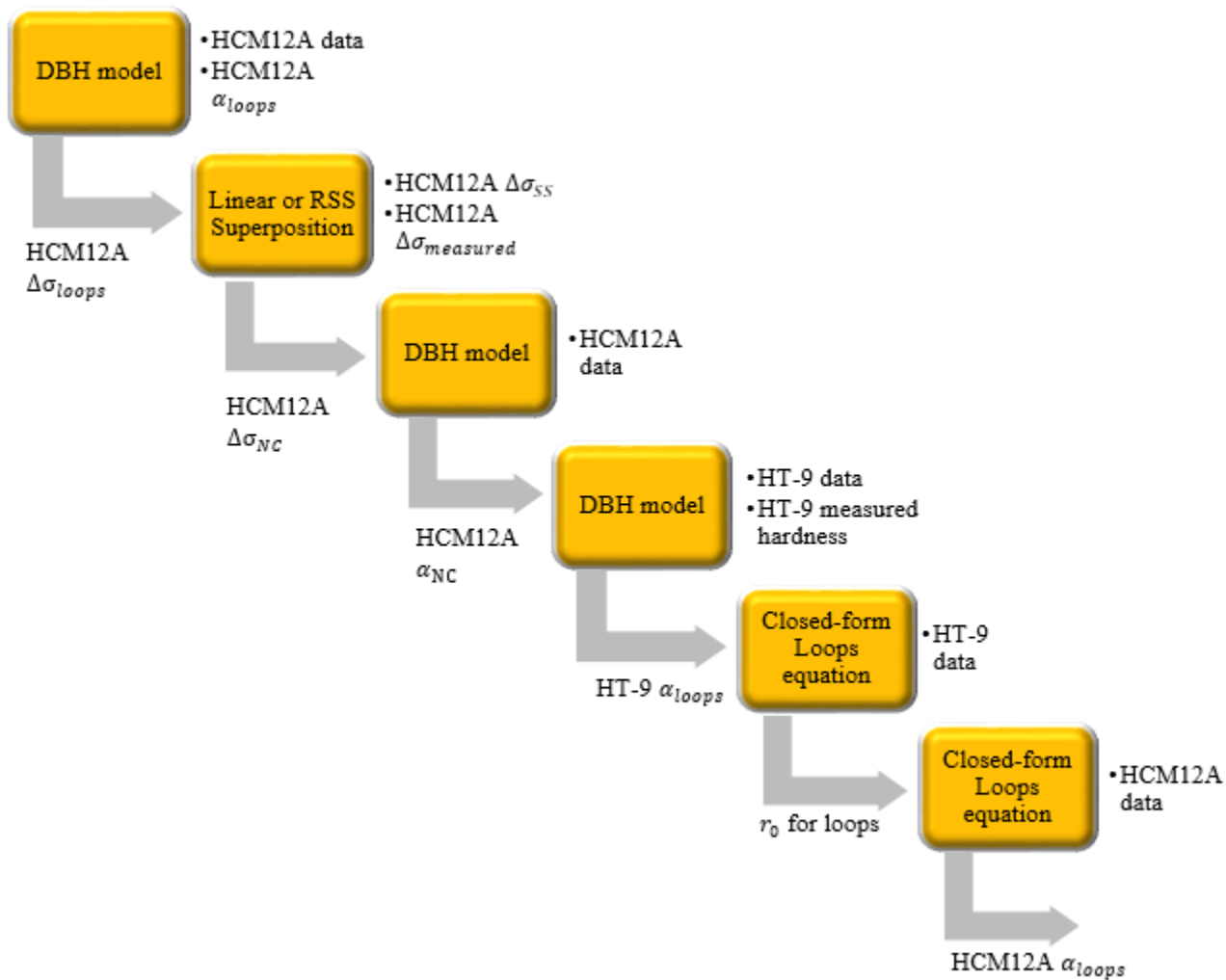
Figure 5.5. Flowchart of analysis for finding strengthening factors for loops and nanoclusters using the DBH model and a closed-form predictive equation for the strengthening factor for loops. Quantities to the right of each box represent the inputs to the equation; quantities below each arrow represent the outputs.

As an alternative to both the linear and RSS methods of superposition, Odette and Lucas [41] suggest a combined approach to finding the total change in yield strength from the component changes. It uses the linear and RSS solutions to the total yield strength as inputs; however, because the total yield strength was a measured rather than predicted value, it would be circular logic to use this approach to infer the component strengths. The equation is:

$$\Delta\sigma_y = S(\Delta\sigma_{y,l} - \Delta\sigma_{y,r}) + \Delta\sigma_{y,r} \tag{16}$$

$$S = \alpha_s - 5\alpha_w + 3.3\alpha_s\alpha_w \tag{17}$$

where α_s is the barrier strength of the strongest type of obstacle and α_w is the strength of the weakest. Because the component yield stresses due to damage features were determined originally using either the linear or RSS methods, it is circular to back-solve this equation for the alpha values.

The table above summarizes results obtained by using the DBH model, the closed-form equation for loops, and the assumption that r_0 is similar for the two alloys. This approach does not use either of the closed-form predictive equations for nanoclusters, coherent or incoherent. It was possible to find all the strengthening factors without using those equations; however, using the same assumptions, it was possible to investigate these as well, for comparison. When using the r_0 value determined from the solution for loops in HT-9, the closed-form equation for incoherent spherical particles predicts alpha values of 0.562 and 0.599 for the heavy ion- and proton-irradiated HCM12A samples respectively. From the dispersed barrier hardening model, these alpha values would predict an increase in yield strength of 986 and 530 MPa, respectively—values far above the observed change from the nanohardness measurements. Subsequently we conclude that the nanoclusters are coherent; this conclusion is supported by the computation of the critical breakaway angle (ϕ_c). This parameter indicates the maximum angle formed as a dislocation line bends around an obstacle before the line breaks and reforms around it. A value of 90° indicates no opposition to dislocation motion; smaller angles indicated stronger barriers and therefore higher strengthening. The equation for strengthening as a function of critical breakaway angle can be written as [42]:

$$\Delta\sigma_{y,nc} = 1.73\frac{\mu b}{\lambda}\cos\Phi_c \tag{18}$$

where $\Delta\sigma_{y,nc}$ is the component strengthening due to nanoclusters, Φ_c is the critical breakaway angle, and λ is the average distance between nanoclusters, expressed as $\sqrt[3]{N} - d$. For the heavy ion- and

proton-irradiated cases, the critical breakaway angles were 84.9° and 88.1°, respectively. These values indicate that the nanoclusters are a minimal barrier to dislocation motion, and the strength contribution from nanoclusters is small. Therefore it is reasonable to assume that the clusters are coherent and that the dislocations can readily shear through them.

The equation for coherent spherically-shaped precipitates is given as [13]:

$$\alpha_{nc}^{coh} = \frac{0.816\gamma_{cp}d}{\mu b^2 \left(1 - 0.816d\sqrt{Nd}\right)} + 1.7\left(\frac{d}{b}\right)^{1.5}\varepsilon^{1.5} + 0.0054\left(\frac{d}{b}\right)^{0.275}\left(\frac{\Delta\mu}{\mu}\right)^{1.5} \tag{19}$$

where γ_{cp} is the interfacial energy (J/m^2), ε is the lattice parameter mismatch between the nanoclusters and the matrix (defined as $\Delta b/b$), and $\Delta\mu$ is the shear modulus mismatch between the cluster and the rest of the matrix. Even if assumed constant across radiation conditions, these three unknowns cannot be solved for with only two $\Delta\sigma_y$ measurements; however, several other constraints exist. All three values must be real; also the lattice parameter mismatch and the ratio $\Delta\mu/\mu$ are unlikely to be greater than 1, and the interfacial energy must be positive. Given these conditions, however, it can readily be demonstrated that no reasonable solution space exists. By iterating through possible values of any one variable and using either of the two superposition methods to solve for the other two, it can be shown that, if the three variables are assumed constant, the model has no real solutions. This ineffectiveness of the coherent cluster equation to model the data in this study may indicate that at least one of the three unknown variables is changed depending on radiation condition or cluster size or density.

Chapter 6: Conclusions and Future Work

The F-M steel alloys HCM12A and HT-9 are candidates for advanced nuclear fission and fusion reactor fuel cladding and structural element materials, and as such, it is important that their irradiation response is thoroughly understood. The combined effects of nanoclusters, dislocation loops, and solid solution hardening have been analyzed simultaneously. The microstructural defects (nanoclusters and loops) tend to harden the material; they are evaluated using the dispersed barrier hardening model, which predicts an increase in yield stress based on the size and number density of the defects. The resulting hardening components due to the two defect types are combined using superposition. The solid solution hardening is based on the change in composition as a result of irradiation; as alloying elements cluster together and separate from the bulk material, the chemical composition of the matrix is changed. A basic linear equation describes the resulting component hardening due to each of several alloying elements, and the reduction of the concentration of these elements in the matrix actually causes it to soften. This softening effect, which was present in the HCM12A but not the HT-9, is combined with the hardening due to microstructural defects to produce the total change in hardness.

At the radiation exposure levels and surface depths focused on in this study, iron ion irradiation increases the hardness more than proton irradiation. According to the SRIM prediction, the ion-irradiated material accumulates higher amounts of damage at shallower levels for a given radiation dose. The actual damage level varies with depth, but for consistency, both samples were nanoindented and evaluated at the same depth.

In this analysis, it was found that the hardening from nanoclusters is the dominant effect in the Fe^{2+}-irradiated HCM12A, but that the hardening from the loops is a stronger effect in the proton irradiated samples. In both cases, however, changes in the solid solution composition and hardness were not a negligible or insignificant consideration. The figure below summarizes the component yield strength changes and strengthening factors for these two alloys.
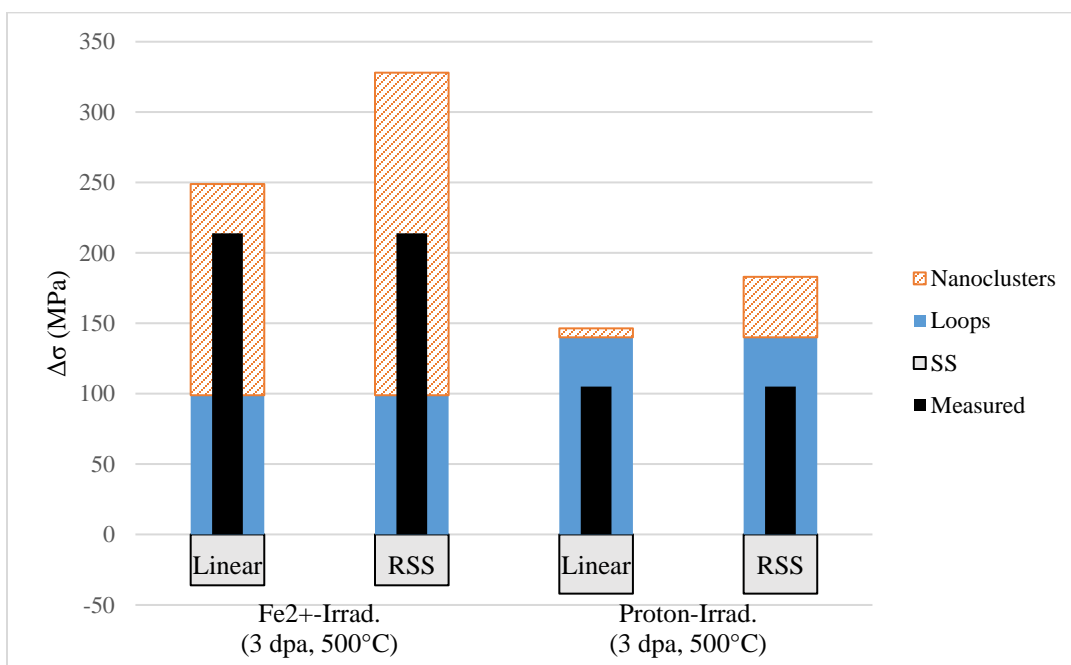
Figure 6.1. Component changes in hardness from loops, nanoclusters, and solid solution softening shown against the total measured change.

Finally, this study shows that the nanoclusters present in irradiated HCM12A can be best described using a coherent particle model. A particle that is incoherent with the surrounding matrix forms a much stronger barrier to dislocation motion; if the particles in these samples were incoherent, the observed strengthening would have been much higher. The incoherent model predicts higher strengthening than was observed, and the calculations of the low critical breakaway angle Φ_c (85° to 88°) reinforce this conclusion.

One area for further research is the determination of the other three variables in the coherent particle model—the interfacial energy γ_{cp}, the lattice parameter mismatch ε, and the shear modulus mismatch $\Delta\mu$. If enough samples at different radiation conditions were characterized for hardness and microstructural changes, these variables could be solved for mathematically. It seems likely, however, that these values are non-constant; they probably vary between irradiation conditions, perhaps as a function of particle size or specific composition.

References

[1]   A. Zeman, L. Debarberis, J. Kočík, V. Slugeň, and E. Keilová, "Microstructural analysis of candidate steels pre-selected for new advanced reactor systems," *Journal of Nuclear Materials*, vol. 362, no. 2, pp. 259–267, May 2007.

[2]   G. S. Was *et al.*, "Emulation of reactor irradiation damage using ion beams," *Scripta Materialia*, vol. 88, pp. 33–36, Oct. 2014.

[3]   R. L. Klueh and D. R. Harries, *High-chromium ferritic and martensitic steels for nuclear applications*. W. Conshohocken, PA: ASTM, 2001.

[4]   J. Z. Briggs, T. D. Parker, and Climax Molybdenum Company., *The super 12% Cr steels*. New York, N.Y.: Climax Molybdenum Co., 1965.

[5]   M. J. Swenson and J. P. Wharry, "Nanocluster irradiation evolution in Fe-9%Cr ODS and ferritic-martensitic alloys," *Journal of Nuclear Materials*, vol. 496, pp. 24–40, Dec. 2017.

[6]   M. J. Swenson and J. P. Wharry, "TEM characterization of irradiated microstructure of Fe-9%Cr ODS and ferritic-martensitic alloys," *Journal of Nuclear Materials*, vol. 502, pp. 30–41, Apr. 2018.

[7]   E. Aydogan, J. S. Weaver, S. A. Maloy, O. El-Atwani, Y. Q. Wang, and N. A. Mara, "Microstructure and mechanical properties of FeCrAl alloys under heavy ion irradiations," *Journal of Nuclear Materials*, vol. 503, pp. 250–262, May 2018.

[8]   O. El-Atwani *et al.*, "Nanohardness measurements of heavy ion irradiated coarse- and nanocrystalline-grained tungsten at room and high temperature," *Journal of Nuclear Materials*, vol. 509, pp. 276–284, Oct. 2018.

[9]   T. Jayakumar, M. D. Mathew, and K. Laha, "High Temperature Materials for Nuclear Fast Fission and Fusion Reactors and Advanced Fossil Power Plants," *Procedia Engineering*, vol. 55, pp. 259–270, 2013.

[10]   G. S. Was, *Fundamentals of Radiation Materials Science: Metals and Alloys*. Springer Berlin Heidelberg, 2007.

[11]   Z. Jiao, V. Shankar, and G. S. Was, "Phase stability in proton and heavy ion irradiated ferritic–martensitic alloys," *Journal of Nuclear Materials*, vol. 419, no. 1, pp. 52–62, Dec. 2011.

[12]   Y. Dai, V. Krsjak, V. Kuksenko, and R. Schäublin, "Microstructural changes of ferritic/martensitic steels after irradiation in spallation target environments," *Journal of Nuclear Materials*, vol. 511, pp. 508–522, Dec. 2018.

[13]   L. Tan and J. T. Busby, "Formulating the strength factor α for improved predictability of radiation hardening," *Journal of Nuclear Materials*, vol. 465, pp. 724–730, Oct. 2015.

[14]   Y. Cui, G. Po, and N. M. Ghoniem, "A coupled dislocation dynamics-continuum barrier field model with application to irradiated materials," *International Journal of Plasticity*, vol. 104, pp. 54–67, May 2018.

[15]   O. Wouters, *Plasticity in Aluminum Alloys at Various Length Scales*. 2006.

[16]   R. E. Stoller and S. J. Zinkle, "On the relationship between uniaxial yield strength and resolved shear stress in polycrystalline materials," *Journal of Nuclear Materials*, vol. 283–287, pp. 349–352, Dec. 2000.

[17]   J. T. Busby, M. C. Hash, and G. S. Was, "The relationship between hardness and yield stress in irradiated austenitic and ferritic steels," *Journal of Nuclear Materials*, vol. 336, no. 2–3, pp. 267–278, Feb. 2005.

[18]   I. Kubena, B. Fournier, and T. Kruml, "Effect of microstructure on low cycle fatigue properties of ODS steels," *Journal of Nuclear Materials*, vol. 424, no. 1, pp. 101–108, May 2012.

[19]   J. Gao, K. Yabuuchi, and A. Kimura, "Ion-irradiation hardening and microstructural evolution in F82H and ferritic alloys," *Journal of Nuclear Materials*, vol. 515, pp. 294–302, Mar. 2019.

[20] M. Matijasevic and A. Almazouzi, "Effect of Cr on the mechanical properties and microstructure of Fe–Cr model alloys after n-irradiation," *Journal of Nuclear Materials*, vol. 377, no. 1, pp. 147–154, Jun. 2008.

[21] M. I. Zakharova, N. A. Artemov, and D. V. Petrov, "Elastic modules and thermal conductivity of neutron irradiated type 13Cr☐2Mo☐Nb☐V☐B ferritic—martensitic steel," *Journal of Nuclear Materials*, vol. 233–237, pp. 280–284, Oct. 1996.

[22] M. J. Swenson, C. K. Dolph, and J. P. Wharry, "The effects of oxide evolution on mechanical properties in proton- and neutron-irradiated Fe-9%Cr ODS steel," *Journal of Nuclear Materials*, vol. 479, pp. 426–435, Oct. 2016.

[23] C. K. Dolph, D. J. da Silva, M. J. Swenson, and J. P. Wharry, "Plastic zone size for nanoindentation of irradiated Fe–9%Cr ODS," *Journal of Nuclear Materials*, vol. 481, pp. 33–45, Dec. 2016.

[24] U. Kanders and K. Kanders, "Strain hardening-softening oscillations induced by nanoindentation in bulk solids," *arXiv:1609.09791 [cond-mat]*, Sep. 2016.

[25] Y.-F. Jia, Y.-Y. Cui, F.-Z. Xuan, and F. Yang, "Comparison between single loading–unloading indentation and continuous stiffness indentation," *RSC Advances*, vol. 7, no. 57, pp. 35655–35665, 2017.

[26] A. Kareer, A. Prasitthipayong, D. Krumwiede, D. M. Collins, P. Hosemann, and S. G. Roberts, "An analytical method to extract irradiation hardening from nanoindentation hardness-depth curves," *Journal of Nuclear Materials*, vol. 498, pp. 274–281, Jan. 2018.

[27] T. R. Allen *et al.*, "Microstructural development in advanced ferritic–martensitic steel HCM12A," *Journal of Nuclear Materials*, vol. 351, no. 1–3, pp. 174–186, Jun. 2006.

[28] F. Bergner, C. Pareige, M. Hernández-Mayoral, L. Malerba, and C. Heintze, "Application of a three-feature dispersed-barrier hardening model to neutron-irradiated Fe–Cr model alloys," *Journal of Nuclear Materials*, vol. 448, no. 1–3, pp. 96–102, May 2014.

[29] C. Heintze, F. Bergner, and M. Hernández-Mayoral, "Ion-irradiation-induced damage in Fe–Cr alloys characterized by nanoindentation," *Journal of Nuclear Materials*, vol. 417, no. 1–3, pp. 980–983, Oct. 2011.

[30] S. I. Porollo, A. M. Dvoriashin, A. N. Vorobyev, and Yu. V. Konobeev, "The microstructure and tensile properties of Fe–Cr alloys after neutron irradiation at 400°C to 5.5–7.1 dpa," *Journal of Nuclear Materials*, vol. 256, no. 2–3, pp. 247–253, Aug. 1998.

[31] A. C. Fischer-Cripps, "Critical review of analysis and interpretation of nanoindentation test data," *Surface and Coatings Technology*, vol. 200, no. 14–15, pp. 4153–4165, Apr. 2006.

[32] W. C. Oliver and G. M. Pharr, "An improved technique for determining hardness and elastic modulus using load and displacement sensing indentation experiments," *Journal of Materials Research*, vol. 7, no. 6, pp. 1564–1583, Jun. 1992.

[33] A. C. Fischer-Cripps, *Nanoindentation*. Springer New York, 2011.

[34] J. P. Wharry, Z. Jiao, V. Shankar, J. T. Busby, and G. S. Was, "Radiation-induced segregation and phase stability in ferritic–martensitic alloy T 91," *Journal of Nuclear Materials*, vol. 417, no. 1–3, pp. 140–144, Oct. 2011.

[35] D. L. Krumwiede, T. Yamamoto, T. A. Saleh, S. A. Maloy, G. R. Odette, and P. Hosemann, "Direct comparison of nanoindentation and tensile test results on reactor-irradiated materials," *Journal of Nuclear Materials*, vol. 504, pp. 135–143, Jun. 2018.

[36] Y. F. Zhang *et al.*, "Radiation-hardening and nano-cluster formation in neutron-irradiated 9Cr 2W low activation steels with different Si contents," *Journal of Nuclear Materials*, vol. 517, pp. 1–8, Apr. 2019.

[37] Q. Lu, W. Xu, and S. van der Zwaag, "Designing new corrosion resistant ferritic heat resistant steel based on optimal solid solution strengthening and minimisation of undesirable

microstructural components," *Computational Materials Science*, vol. 84, pp. 198–205, Mar. 2014.

[38] F. B. Pickering, *Physical metallurgy and the design of steels*, vol. 63. Applied Science Publishers London, 1978.

[39] Z. Jiao and G. S. Was, "Precipitate evolution in ion-irradiated HCM12A," *Journal of Nuclear Materials*, vol. 425, no. 1–3, pp. 105–111, Jun. 2012.

[40] K. G. Field, X. Hu, K. C. Littrell, Y. Yamamoto, and L. L. Snead, "Radiation tolerance of neutron-irradiated model Fe–Cr–Al alloys," *Journal of Nuclear Materials*, vol. 465, pp. 746–755, Oct. 2015.

[41] G. R. Odette and G. E. Lucas, "Recent progress in understanding reactor pressure vessel steel embrittlement," *Radiation Effects and Defects in Solids*, vol. 144, no. 1–4, pp. 189–231, Jun. 1998.

[42] A. Xu *et al.*, "Ion-irradiation-induced clustering in W–Re and W–Re–Os alloys: A comparative study using atom probe tomography and nanoindentation measurements," *Acta Materialia*, vol. 87, pp. 121–127, Apr. 2015.